

# The correlation of extragalactic $\gamma$ -rays with cosmic matter density distributions from weak-gravitational lensing

Masato Shirasaki,<sup>1,\*</sup> Oscar Macias,<sup>2,†</sup> Shunsaku Horiuchi,<sup>2,‡</sup>  
Naoki Yoshida,<sup>3,4,§</sup> Chien-Hsiu Lee,<sup>5</sup> and Atsushi J. Nishizawa<sup>6</sup>

<sup>1</sup>*National Astronomical Observatory of Japan (NAOJ), Mitaka, Tokyo 181-8588, Japan*

<sup>2</sup>*Center for Neutrino Physics, Department of Physics,  
Virginia Tech, Blacksburg, Virginia 24061, USA*

<sup>3</sup>*Department of Physics, University of Tokyo, Tokyo 113-0033, Japan*  
*Kavli Institute for the Physics and Mathematics of the Universe (WPI),  
University of Tokyo, Kashiwa, Chiba 277-8583, Japan*

<sup>4</sup>*CREST, Japan Science and Technology Agency,  
4-1-8 Honcho, Kawaguchi, Saitama, 332-0012, Japan*

<sup>5</sup>*Subaru Telescope, NAOJ, 650 N Aohoku Pl. Hilo, HI 96720, USA*

<sup>6</sup>*Institute for Advanced Research, Nagoya University, Nagoya 464-8602, Aichi, Japan*

The extragalactic  $\gamma$ -ray background (EGB) arises from the accumulation of  $\gamma$ -ray emissions from resolved and unresolved extragalactic sources as well as diffuse processes. It is important to study the statistical properties of the EGB in the context of cosmological structure formation. Known astrophysical  $\gamma$ -ray sources such as blazars, star-forming galaxies, and radio galaxies are expected to trace the underlying cosmic matter density distribution. We explore the correlation of the EGB from Fermi-LAT data with the large-scale matter density distribution from the Subaru Hyper Suprime-Cam (HSC) SSP survey. We reconstruct an unbiased surface matter density distribution  $\kappa$  at  $z \lesssim 1$  by applying weak-gravitational lensing analysis to the first-year HSC data. We then calculate the  $\gamma - \kappa$  cross-correlation. Our measurements are consistent with a null detection, but a weak correlation is found at angular scales of 30-60 arcmin, especially when distant source galaxies at  $z > 1$  are used for the lensing  $\kappa$  reconstruction. The large-scale correlation suggests strong clustering of high-redshift  $\gamma$ -ray sources such as blazars. However, the inferred bias factor of 4 – 5 is larger by about a factor of two than results from other clustering analyses. The final HSC data covering 1,400 squared degrees will play an essential role to determine accurately the blazar bias at  $z > 0.5$ .

## I. INTRODUCTION

Since its discovery, extragalactic  $\gamma$  rays have been one of the most important subjects in high-energy astrophysics [1]. The extragalactic gamma-ray background (EGB) is partly explained by  $\gamma$ -ray emission from resolved point sources outside the Milky Way. The Large Area Telescope (LAT) onboard the Fermi Gamma-ray Space Telescope has detected  $\gamma$ -ray sources from across the whole sky [2]. Many of them are extragalactic, and hence contribute to the EGB. In addition to the resolved contributions, a diffuse and nearly isotropic emission, referred to as the isotropic gamma-ray background (IGRB), is necessary to provide a better fit to the EGB observations [3, 4] (also see Ref. [5] for a recent review of the IGRB). Although the origin of the IGRB is still under debate, a significant fraction may originate from the emission from unresolved astrophysical sources, which are too faint to be detected on an individual basis. Possible candidates include blazars [6, 7], star-forming galaxies [8, 9], and radio galaxies [10, 11].

Recently, Ref. [4] measured the energy spectrum of the

EGB in the range between 0.1 GeV to 820 GeV and showed that the EGB spectrum is well described by a power law with a photon index of  $2.32 (\pm 0.02)$  and an exponential cut off of  $279 (\pm 52)$  GeV. Improved modeling of a linear combination of astrophysical  $\gamma$ -ray sources based on Fermi-LAT data can provide an adequate interpretation of the origin of the EGB. Ref. [12] showed that the cumulative emission of blazars, star-forming galaxies, and radio galaxies can explain the EGB spectrum in the range 0.1–820 GeV with the cut off originating from the expected  $\gamma$ -ray attenuation by the extragalactic background light [13].

In the standard model of cosmic structure formation, galactic-size astrophysical sources are hosted by dark matter halos. Therefore, the spatial distribution of EGB emission is expected to be correlated with the underlying matter density distribution of the Universe [14, 15]. There already exist several pieces of supporting evidence that show such a correlation between the EGB and large-scale structure (LSS) tracers. For example, Ref. [16] find spatial clustering of resolved blazars detected in the 2-year all-sky survey by Fermi-LAT. The cross correlations between IGRB and galaxies [17] and galaxy clusters [18] have been also detected. However, these previous studies do not provide direct information on the relation between the EGB and the cosmic matter density, because the tracers of LSS that have been used are known to be *biased* with respect to the underlying matter density.

---

\* masato.shirasaki@nao.ac.jp

† oscar.macias@vt.edu

‡ horiuchi@vt.edu

§ naoki.yoshida@ipmu.jp

Fortunately, gravitational lensing provides a physical and *unbiased* probe of the cosmic matter density [19]. It is free from assumptions that relate the matter density to observable quantities. By contrast, e.g., for galaxies to be used as a tracer of large-scale structure, some assumption needs to be made on the relation between the galaxy luminosity and mass, and even additional conditions need to be invoked such as hydrostatic equilibrium.

The correlation between the IGRB and large-scale matter distribution has been detected using gravitational lensing of the cosmic microwave background (CMB), reported in Ref. [20]. In the concordance  $\Lambda$ CDM cosmology, the CMB lensing effect is largely determined by the matter density distribution at redshift  $z = 2 - 3$  [21]. Thus, it is still unclear whether there exists a strong correlation between the EGB and cosmic matter density at  $z \lesssim 1$ . Since extragalactic sources at lower redshift should appear brighter, a large fraction of the EGB is expected to originate from the structures (sources) at  $z \lesssim 1$ . This fact further motivates to use cross-correlation analysis of the EGB with low-redshift structures.

In this paper, we explore the correlation between the EGB and the cosmic matter density distribution probed by an optical weak lensing survey. We achieve this by using galaxy imaging data taken from the Subaru Hyper-Suprime Cam (HSC) SSP survey. Unlike similar investigations in the literature [22–24], we work with the reconstructed surface matter density from the galaxy imaging data, i.e., lensing convergence. We then perform, for the first time, the cross-correlation analysis of the EGB (including all the resolved components) and the lensing convergence. Our measurement can provide direct evidence of the correlation between the extragalactic  $\gamma$ -rays and cosmic matter density at  $z \lesssim 1$ . It also enables us to study the *clustering* properties of the EGB, and provides invaluable information on the EGB sources that cannot be extracted from mean intensity analyses. We expect that the correlation depends on the clustering of extragalactic  $\gamma$ -ray sources at redshifts of  $z \sim 0.5$ . Since it is difficult to measure the auto-correlation of  $\gamma$ -ray sources as a function of redshift because of the significantly low number density of known sources, our measurement will be complementary to other analyses and give important implications for the nature of the EGB.

The paper is organized as follows. In Section II, we summarize the basics of EGB and gravitational lensing. In Section III, we describe the galaxy-imaging and  $\gamma$ -ray data used, and provide details of the cross-correlation analysis. Our benchmark model of the cross correlation is discussed in Section IV. In Section V, we show the result of our cross-correlation analysis, and discuss constraints on possible connection between astrophysical  $\gamma$ -ray sources and LSS. Concluding remarks and discussions are given in Section VI. Throughout, we use the standard cosmological parameters  $H_0 = 100h \text{ km s}^{-1}$  with  $h = 0.7$ , the average matter density  $\Omega_{\text{m}0} = 0.279$ , the cosmological constant  $\Omega_\Lambda = 0.721$ , and the amplitude of matter density fluctuations within  $8 h^{-1} \text{ Mpc}$ ,  $\sigma_8 = 0.821$ .

## II. OBSERVABLES

### A. Extragalactic gamma-ray background

The  $\gamma$ -ray intensity along a given direction  $\boldsymbol{\theta}$  can be written as [15],

$$I_\gamma(\boldsymbol{\theta}) = \int d\chi W_g(\chi) g(r(\chi)\boldsymbol{\theta}, \chi), \quad (1)$$

where  $\chi(z)$  denotes the radial comoving distance (function of redshift  $z$ ),  $r(\chi)$  is the comoving angular diameter distance,  $g(\boldsymbol{x})$  is the relevant density field of the  $\gamma$ -ray source, and  $W_g(\chi)$  is the window function. In this paper, we define  $W_g(\chi)$  so that the mean  $\gamma$ -ray intensity can be expressed as,

$$\langle I_\gamma \rangle = \int d\chi W_g(\chi), \quad (2)$$

where  $\langle \dots \rangle$  represents an averaged quantity over the sky.

Suppose that an astrophysical source population  $X$  can emit  $\gamma$  rays, we set the relevant field in Eq. (1) to be  $g(\boldsymbol{x}) \propto L_\gamma \delta^{(3)}(\boldsymbol{x})$  where  $L_\gamma$  denotes the  $\gamma$ -ray intensity emitted from sources,  $\delta^{(3)}(\boldsymbol{x})$  is the dirac delta function in three-dimensional space and we assume any source populations can be approximated as point source<sup>1</sup>. In terms of the luminosity function, the window function  $W_g$  for the source population  $X$  can be written as [14, 25],

$$\begin{aligned} W_{g,X}(\chi) = & \int_{E_{\text{min}}}^{E_{\text{max}}} \frac{dE_\gamma}{4\pi} e^{-\tau(E'_\gamma, z(\chi))} \\ & \times \int_{\Gamma_{\text{min}}}^{\Gamma_{\text{max}}} d\Gamma_X \mathcal{A}(z(\chi), \Gamma_X) \frac{dN_{\gamma,X}(E_\gamma, z(\chi), \Gamma_X)}{dE_\gamma} \\ & \times \int_{L_{\text{min}}}^{L_{\text{max}}} dL_\gamma L_\gamma \Phi_X(L_\gamma, z(\chi), \Gamma_X), \end{aligned} \quad (3)$$

where  $E_\gamma$  is the observed  $\gamma$ -ray energy,  $E'_\gamma = (1+z)E_\gamma$  is the energy of the  $\gamma$  ray at redshift  $z$ ,  $dN_{\gamma,X}/dE_\gamma$  is the  $\gamma$ -ray spectrum,  $\Gamma_X$  is the photon spectrum index,  $\Phi_X(L_\gamma, z, \Gamma_X)$  is the  $\gamma$ -ray luminosity function, and the exponential factor in the integral takes into account the effect of  $\gamma$ -ray attenuation during propagation owing to pair creation on diffuse extragalactic photons. For the  $\gamma$ -ray optical depth  $\tau(E'_\gamma, z)$ , we adopt the model in Ref. [26]. The factor  $\mathcal{A}$  in Eq. (3) accounts for the conversion normalisation between the emitted and observed  $\gamma$ -ray energies including k-correction, and depends on the source spectral index and the energy range considered.

In the following, we summarize the basic quantities to compute the  $\gamma$ -ray intensity using Eq. (3) for several astrophysical  $\gamma$ -ray sources.

<sup>1</sup> This approximation should be valid as long as we focus on the correlation with the scale much larger than the actual size of astrophysical sources. The angular scales of interest in this paper is set to be larger than 30 arcmins.

### 1. Blazars

Following Ref. [12], we characterize the blazar population by means of a parametric description of their  $\gamma$ -ray luminosity function and energy spectrum. The blazer  $\gamma$ -ray luminosity function is defined as the number of sources per unit luminosity  $L_\gamma$  (defined in the rest frame of the source, for energies between 0.1 and 100 GeV). The luminosity function at  $z = 0$  is modeled as,

$$\Phi_b(L_\gamma, z = 0, \Gamma_b) = \frac{A}{\ln 10 L_\gamma} \left[ \left( \frac{L_\gamma}{L_*} \right)^{\gamma_a} + \left( \frac{L_\gamma}{L_*} \right)^{\gamma_b} \right]^{-1} \times e^{-[\Gamma_b - \mu(L_\gamma)]^2 / 2\sigma^2}, \quad (4)$$

where the parameters of  $A$ ,  $\gamma_a$ ,  $\gamma_b$ ,  $L_*$ ,  $\sigma$  and the relation of  $\mu(L_\gamma)$  have been calibrated with Fermi-LAT resolved blazars for a given redshift-evolution scenario [12]. We assume that the redshift evolution of the luminosity function is expressed in the following form,

$$\Phi_b(L_\gamma, z, \Gamma_b) = f_e(z, L_\gamma) \Phi_b(L_\gamma, z = 0, \Gamma_b), \quad (5)$$

$$f_e(z, L_\gamma) = \left[ \left( \frac{1+z}{1+z_c(L_\gamma)} \right)^{-p_1(L_\gamma)} + \left( \frac{1+z}{1+z_c(L_\gamma)} \right)^{-p_2(L_\gamma)} \right]^{-1}, \quad (6)$$

where  $z_c$ ,  $p_1$  and  $p_2$  are assumed to depend on the  $\gamma$ -ray luminosity. We use the same parameter values as in Ref. [12] in Eqs. (4) and (6). This model is called the luminosity-density dependent evolution scenario.

Blazars are known to have a characteristic, broad energy spectrum. We follow the  $\gamma$ -ray energy spectrum proposed in Ref. [12],

$$\frac{dN_{\gamma,b}}{dE_\gamma} = K \left[ \left( \frac{E_\gamma}{E_b(\Gamma_b)} \right)^a + \left( \frac{E_\gamma}{E_b(\Gamma_b)} \right)^b \right]^{-1}, \quad (7)$$

where  $\log(E_b/1 \text{ GeV}) = 9.25 - 4.11\Gamma_b$  and we determine the normalization factor  $K$  so that  $L_\gamma$  can be defined in the energy range of 0.1-100 GeV. We set  $\mathcal{A} = (1+z)^{-\Gamma_b}$  to include the k-correction. When computing the  $\gamma$ -ray intensity from blazars, we adopt  $\Gamma_{\min} = 1$ ,  $\Gamma_{\max} = 3.5$ ,  $L_{\min} = 10^{43} \text{ erg s}^{-1}$ , and  $L_{\max} = 10^{52} \text{ erg s}^{-1}$ .

Note that the above model of  $\Phi_b(L_\gamma, z, \Gamma_b)$  and  $dN_{\gamma,b}/dE_\gamma$  can reasonably explain the Fermi-LAT data of resolved blazars. The expected contribution to the mean EGB intensity above  $\sim 1 \text{ GeV}$  will be  $\sim 60 - 70\%$  [12].

### 2. Star-forming galaxies

For star-forming galaxies, we assume the power-law energy spectrum  $dN_{\gamma,s}/dE_\gamma \propto E_\gamma^{-2.2}$ , characteristic of the LAT-detected starburst galaxies [27]. We obtain the luminosity function by scaling from the infrared luminosity

function of galaxies measured in Ref. [28]. The conversion of the infrared luminosity to the gamma-ray luminosity of the galaxies is given by

$$\log \left( \frac{L_\gamma}{\text{erg s}^{-1}} \right) = 1.17 \log \left( \frac{L_{\text{IR}}}{10^{10} L_\odot} \right) + 39.28, \quad (8)$$

where  $L_\gamma$  is defined in the range of 0.1-100 GeV in observer's frame and  $L_{\text{IR}}$  is the infrared luminosity for 8-1000  $\mu\text{m}$  [27]. According to the definition of  $L_\gamma$ , we set  $\mathcal{A} = (1+z)^{-2}$ . We adopt  $L_{\min} = 10^{30} \text{ erg s}^{-1}$  and  $L_{\max} = 10^{43} \text{ erg s}^{-1}$ .

### 3. Radio galaxies

For radio galaxies, we follow the model of Ref. [11], which has established a correlation between the  $\gamma$ -ray luminosity and the radio-core luminosity  $L_{r,\text{core}}$  at 5 GHz. Using the correlation together with the radio luminosity function [29], one can evaluate the contribution to the EGB from radio galaxies. We consider the best-fit  $L_\gamma - L_{r,\text{core}}$  relation from Ref. [11],

$$\log \left( \frac{L_\gamma}{\text{erg s}^{-1}} \right) = 1.008 \log \left( \frac{L_{r,\text{core}}}{\text{erg s}^{-1}} \right) + 2.00, \quad (9)$$

where  $L_\gamma$  is defined between 0.1 and 100 GeV in observer's frame. We assume an average spectral index of 2.37 throughout this paper, and set  $\mathcal{A} = (1+z)^{-2}$ .  $L_{\min} = 10^{41} \text{ erg s}^{-1}$  and  $L_{\max} = 10^{49} \text{ erg s}^{-1}$  are adopted in Eq. (3).

## B. Gravitational lensing

### 1. Basics

The weak gravitational lensing effect is commonly characterized by the distortion of image of a source object (galaxy) by the following  $2 \times 2$  matrix,

$$A_{ij} = \frac{\partial x_{\text{true}}^i}{\partial x_{\text{obs}}^j} \equiv \begin{pmatrix} 1 - \kappa - \gamma_1 & -\gamma_2 - \omega \\ -\gamma_2 + \omega & 1 - \kappa + \gamma_1 \end{pmatrix}, \quad (10)$$

where we denote the observed position of a source object as  $\mathbf{x}_{\text{obs}}$  and the true position as  $\mathbf{x}_{\text{true}}$ . In the above equation,  $\kappa$  is the convergence,  $\gamma$  is the shear, and  $\omega$  is the rotation. In the weak lensing regime ( $\kappa, \gamma \ll 1$ ), one can relate the convergence field to the density contrast of underlying matter density field  $\delta_m(\mathbf{x})$  [19],

$$\kappa(\boldsymbol{\theta}) = \int_0^\infty d\chi W_\kappa(\chi) \delta_m(r(\chi)\boldsymbol{\theta}, \chi), \quad (11)$$

$$W_\kappa(\chi) = \frac{3}{2} \left( \frac{H_0}{c} \right)^2 \Omega_{\text{m}0} (1+z(\chi)) r(\chi) \times \int_\chi^\infty d\chi' p(\chi') \frac{r(\chi' - \chi)}{r(\chi')}, \quad (12)$$

where  $p(\chi)$  represents the source distribution normalized to  $\int d\chi p(\chi) = 1$ .

## 2. Reconstruction of convergence field

In optical imaging surveys, galaxies' ellipticities are commonly used to estimate the shear component  $\gamma$  in Eq. (10). Since each component in the tensor  $A_{ij}$  can be expressed as the second derivative of the gravitational potential, one can reconstruct the convergence field from the observed shear field in Fourier space as

$$\hat{\kappa}(\boldsymbol{\ell}) = \frac{\ell_1^2 - \ell_2^2}{\ell_1^2 + \ell_2^2} \hat{\gamma}_1(\boldsymbol{\ell}) + \frac{2\ell_1\ell_2}{\ell_1^2 + \ell_2^2} \hat{\gamma}_2(\boldsymbol{\ell}), \quad (13)$$

where  $\hat{\kappa}$  and  $\hat{\gamma}$  are the convergence and shear in Fourier space, and  $\boldsymbol{\ell}$  is the wave vector with components  $\ell_1$  and  $\ell_2$  [30].

For a given source galaxy, one considers the relation between the observed ellipticity  $e_{\text{obs},\alpha}$  and the expected shear  $\tilde{\gamma}_\alpha$ ,

$$\tilde{\gamma}_\alpha = \frac{e_{\text{obs},\alpha}}{2\mathcal{R}}, \quad (14)$$

$$\tilde{\gamma}_\alpha = (1 + m)\gamma_{\text{true},\alpha} + c_\alpha, \quad (15)$$

where  $\mathcal{R}$  is the conversion factor to represent the response of the distortion of the galaxy image to a small shear [31],  $\gamma_{\text{true},\alpha}$  is the true value of cosmic shear, and  $m$  and  $c_\alpha$  are the multiplicative and additive biases to assess possible systematic uncertainty in galaxy shape measurements. In practice, before employing the conversion in Eq. (13), one must first construct the smoothed shear field on grids [32],

$$\gamma_{\text{sm},\alpha}(\boldsymbol{\theta}) = \frac{\sum_i w_i (\tilde{\gamma}_{i,\alpha} - c_{i,\alpha}) W(\boldsymbol{\theta} - \boldsymbol{\theta}_i)}{\sum_i w_i (1 + m_i) W(\boldsymbol{\theta} - \boldsymbol{\theta}_i)}, \quad (16)$$

where  $\boldsymbol{\theta}_i$  locates the position of the  $i$ -th source galaxy,  $w_i$  represents the inverse variance weight for the  $i$ -th source galaxy, and  $W(\boldsymbol{\theta})$  is assumed to be a Gaussian

$$W(\boldsymbol{\theta}) = \frac{1}{\pi\theta_G^2} \exp\left(-\frac{\theta^2}{\theta_G^2}\right). \quad (17)$$

Using Eqs. (13) and (16), one can derive the smoothed convergence field from the observed imaging data through a Fast Fourier Transform (FFT).

The resulting field is mathematically equivalent to the filtered convergence field [33] which is defined as

$$\kappa_{\text{sm}}(\boldsymbol{\theta}) = \int d^2\phi \kappa(\phi) U_\kappa(\boldsymbol{\theta} - \phi), \quad (18)$$

where the smoothing filter for  $\kappa$  can be expressed as

$$U_\kappa(\theta) = 2 \int_\theta^\infty d\theta' \frac{W(\theta')}{\theta'} - W(\theta). \quad (19)$$

## III. DATA

### A. *Fermi*-LAT

We use  $\sim 7$  years (from August 4, 2008 to September 4, 2015) of Pass 8 ULTRACLEANVETO photons with

reconstructed energy in the 1 – 500 GeV range. Photons detected at zenith angles larger than  $90^\circ$  were excised in order to limit the contamination from  $\gamma$ -rays generated by cosmic-ray interactions in the Earth limb. Moreover, data were filtered removing time periods when the instrument was not in sky-survey mode. *Fermi* Science Tools v10r0p5 and instrument response functions (IRFs) P8R2\_ULTRACLEANVETO\_V6 were used for this analysis. We included photons within a  $20^\circ \times 20^\circ$  square region encompassing each of the HSC fields of view. Figure 1 shows smoothed EGB maps observed by the LAT above 1 GeV (details of the *Fermi*-LAT analysis and data processing are provided in the appendix).

### B. Subaru Hyper-Suprime Cam

Hyper Suprime-Cam (HSC) is a wide-field imaging camera on the prime focus of the 8.2m Subaru telescope [34–37] (also see Kawanomoto, S., et al. 2018 in prep.). Among three layers in the HSC survey, the Wide layer will cover 1400 deg<sup>2</sup> in five broad photometric bands (grizy) over 5–6 years, with excellent image quality of sub-arcsec seeing. In this paper, we use a catalog of galaxy shapes that has been generated for cosmological weak lensing analysis in the first year data release. We denote the data as HSCS16A. The details of galaxy shape measurements and catalog information are found in Ref. [38].

In brief, the HSCS16A shape catalog contains the shapes of  $\sim 12$  million galaxies selected from 137 deg<sup>2</sup> measured with the re-Gaussianization method [39]. The shape measurement is performed in the coadded  $i$ -band image and calibrated by simulated galaxy images similar to those used in GREAT3 [40]. The image simulation enables to carry out reliable shear calibration, since it takes into account realistic HSC PSFs and reproduces the observed distribution of galaxy properties with remarkable accuracy [41]. We apply a conservative galaxy selection criteria for the first year science, e.g.,  $S/N \geq 10$  and  $i \leq 24.5$ , giving an average raw number density of galaxies  $\bar{n} \sim 25$  arcmin<sup>-2</sup>. The HSCS16A dataset consists of 6 patches; XMM, GAMA09H, GAMA15H, HECTOMAP, VVDS, and WIDE12H. While we present convergence maps for these individual patches separately, we combine our results on cross-correlations for all 6 patches. Accurate photometric redshifts in the HSCS16A are suitable for tomographic approach as in Refs. [24, 25]. While photometric redshifts are measured for the HSC galaxies using several different techniques, throughout this paper we use the MLZ photometric redshifts [42]. Individual HSC galaxies have a posterior probability distribution function (PDF) of redshift estimated by MLZ. We define the point estimate of each galaxy's redshift where its PDF takes the maximum. We use the PDF information to evaluate the mean redshift as  $\langle z \rangle = \int dz z \sum_i^{N_{\text{gal}}} P_i(z) / N_{\text{gal}}$ , where  $N_{\text{gal}}$  is the number of source galaxies and  $P_i(z)$  represents the PDF of photometric redshift for  $i$ -th galaxy. When

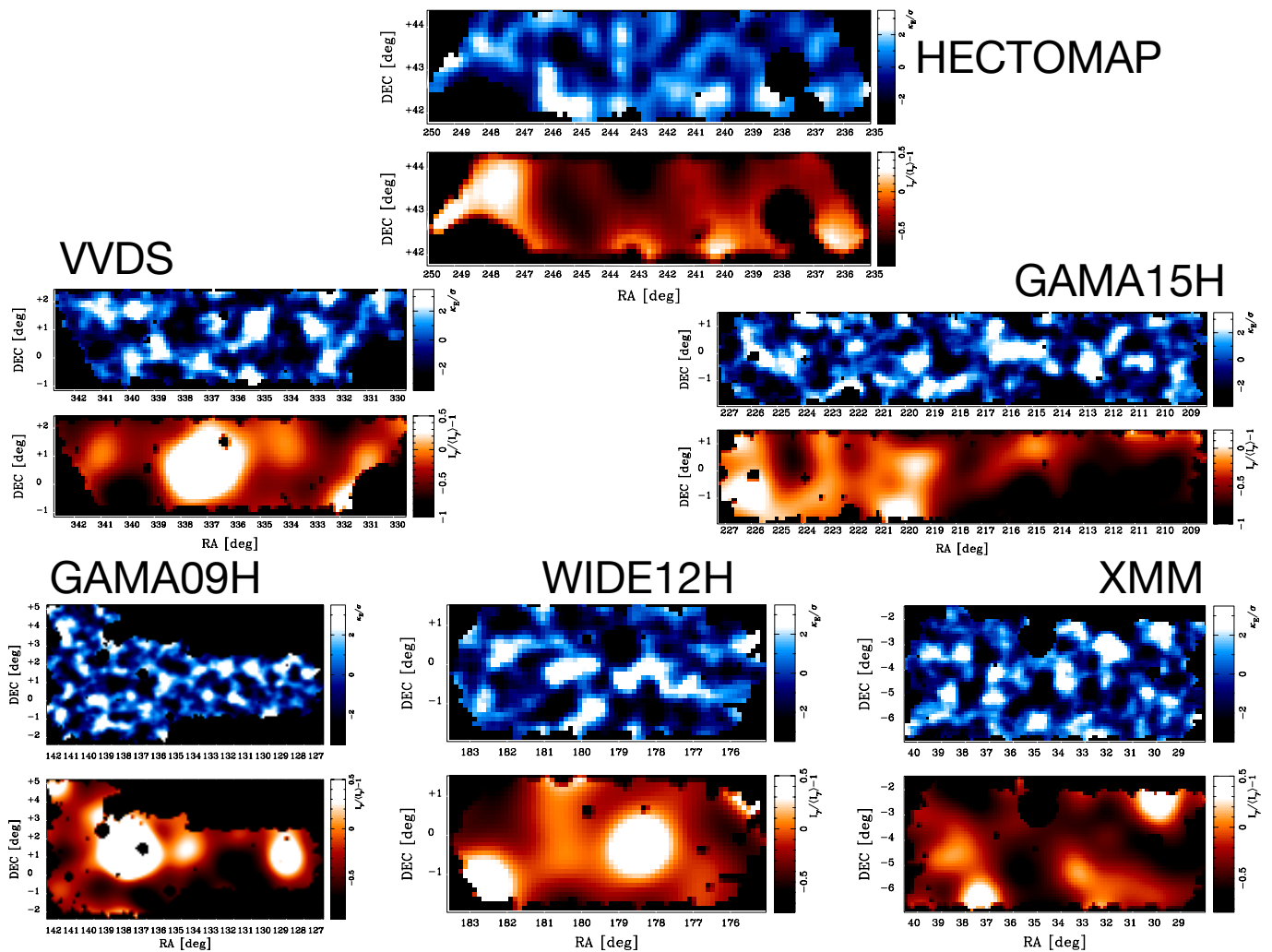


FIG. 1. We plot the smoothed convergence field (upper panels) and extragalactic gamma-ray background intensity (EGB; bottom panels) for 6 HSC patches as labeled. In this figure, we set the smoothing scale to be  $\theta_G = 40$  arcmin in Eq. (17) and use all source galaxies (no photometric redshift selections are applied). We also apply a Gaussian smoothing of 40 arcmin for the EGB maps. Brighter regions correspond to denser in mass or higher in  $\gamma$ -ray intensity, whereas darker regions are for more under-dense in mass or fainter in  $\gamma$ -ray intensity.

using all galaxies in the HSC shape catalog, we obtain the mean source redshift  $z_m = 0.96$ . For our lensing tomography analysis, we divide the source galaxies into three bins using their point estimates  $z_{\text{photo}}$  as  $0.3 < z_{\text{photo}} < 0.8$ ,  $0.8 < z_{\text{photo}} < 1.2$ , and  $1.2 < z_{\text{photo}} < 1.9$ , and the corresponding mean source redshifts are  $z_m = 0.60, 1.00$ , and  $1.42$ , respectively. The true redshift distribution of the source galaxies is commonly approximated as the sum of the PDFs estimated from MLZ. We use the sum as the source redshift distribution in our theoretical model of weak lensing signals (see Eq. [12]).

We then reconstruct the smoothed convergence field from the HSCS16A data as described in Section II B 2. We follow a similar approach to that of Ref. [43]. Adopting a flat-sky approximation, we first create a pixelized shear map for each of the 6 patches on regular grids

with a grid size of 0.1 deg. We then apply the FFT and perform convolution in Fourier space to obtain the smoothed convergence field, which is referred to as the E-mode convergence  $\kappa_E$  in the literature. The imaginary part of the reconstructed convergence corresponds to the B-mode convergence,  $\kappa_B$ , which can be an indicator of the existence of certain types of residual systematics in our weak lensing measurements.

In actual observations, there are missing galaxy shear data due to bright star masks and edges. Applying our method directly to such regions likely generates noisy maps. We thus determine the mask regions for each convergence map by using the smoothed number density map of the input galaxies with the same smoothing kernel as in Eq. (17). Then we mask all pixels with the smoothed galaxy number density less than 0.5 times the

mean number density. In addition, we apply a conservative mask of  $|b| < 30$  deg about the Galactic plane in the cross-correlation analysis presented in Section III C. Basic characteristics of the HSCS16A data are summarized in Table I. Figure 1 shows our reconstructed EGB (bottom panels) and convergence fields (upper panels) when we set the smoothing size of  $\theta_G = 40$  arcmin.

### C. Estimator of cross correlation

In order to measure the  $\kappa - \gamma$  cross-correlation, we introduce the following simple statistic for our smoothed maps,

$$\langle \kappa_E I_\gamma \rangle(\theta_G) \equiv \frac{\sum_i \kappa_{\text{sm}}(\boldsymbol{\theta}_i) I_{\gamma, \text{sm}}(\boldsymbol{\theta}_i)}{\sum_i 1}, \quad (20)$$

with

$$I_{\gamma, \text{sm}}(\boldsymbol{\theta}) = \int d^2\phi I_\gamma(\phi) W(\boldsymbol{\theta} - \phi). \quad (21)$$

Here,  $\kappa_{\text{sm}}(\boldsymbol{\theta}_i)$  represents the smoothed convergence map reconstructed as in Section II B 2 (or defined in Eq. [18]), and the sum in Eq. (20) is taken over all unmasked pixels for individual HSCS16A fields. Hence, the quantity  $\langle \kappa_E I_\gamma \rangle$  is a function of the smoothing scale  $\theta_G$ . It also depends on the photometric-redshift selection of source galaxies in gravitational lensing analysis. We also examine the similar quantity of  $\langle \kappa_B I_\gamma \rangle$  to study residual systematic effects in the galaxy shape measurement.

To estimate the statistical error, we utilize 200 mock shear catalogs for the HSCS16A<sup>2</sup>. We follow the method developed in Refs. [43, 45] to create realistic mock catalogs that incorporate the features of actual data and ray-tracing simulations (also see Ref. [41] and Shirasaki et al. in prep). We use the all-sky ray-tracing simulations of gravitational lensing in Ref. [46]. Each mock data consists of 38 different source planes each separated by a comoving separation of  $\Delta\chi = 150 h^{-1}$  Mpc, covering source planes up to redshift of 5.3. The angular resolution is set to be 0.43 arcmin. We use the observed photometric redshifts and angular positions of real galaxies as in Ref. [43]. In short, we perform the following procedures: (1) we assign each real HSC galaxy to the nearest angular pixel in the nearest redshift source plane, (2) we randomly rotate the orientation of the galaxy to remove the real lensing effect, (3) we simulate the lensing distortion effect at the source position by adding the

local lensing shear and the intrinsic shape, (4) we include the additional variance due to measurement error, and (5) repeat the procedures (1)-(4) for all the source galaxies. Note that, when generating a realization, we randomly sample the source redshift from the posterior PDF of photometric redshift for each galaxy. Our mock catalogs include directly the properties of source galaxies (e.g., magnitudes, ellipticities and spatial variations in the number densities), statistical uncertainties in photometric redshifts, and also the survey geometry. We use 10 full-sky simulations to extract 200 mock HSCS16A catalogs.

For each patch of the HSCS16A data, we evaluate the cross-correlation Eq. (20) and estimate their errors by using the standard deviation from our 200 mock catalogs. Using the measured correlations and the standard deviations for a total of 6 patches, we combine them by the inverse-variance weighted method [23, 43]. The same procedures are also applied to the 200 mock catalogs, in order to estimate the covariance of  $\langle \kappa_E I_\gamma \rangle$  in the HSCS16A among different  $\theta_G$  and source redshift selections. To justify our procedure of combining the cross correlations, we have checked the field variation in EGB mean intensity above 1 GeV and that of the mean redshift of HSC galaxies. We find 20–30% differences in the EGB mean intensity and less than 5% difference in the mean redshift among different patches. These differences are small enough compared to the current statistical uncertainty in the cross correlation measurement.

## IV. ANALYTIC MODEL

### A. Formulation

Here we derive the expectation value of Eq. (20) in the standard structure formation model. Let us begin with the two-point cross-correlation function between  $\kappa_{\text{sm}}$  and  $I_{\gamma, \text{sm}}$  in real space. Under a flat-sky approximation, it is given by

$$\begin{aligned} \langle \kappa_{\text{sm}}(\boldsymbol{\theta}_1) I_{\gamma, \text{sm}}(\boldsymbol{\theta}_2) \rangle &= \int \frac{d^2\ell_1}{(2\pi)^2} \int \frac{d^2\ell_2}{(2\pi)^2} e^{i\ell_1 \cdot \boldsymbol{\theta}_1 - i\ell_2 \cdot \boldsymbol{\theta}_2} \\ &\quad \times \langle \hat{\kappa}_{\text{sm}}(\boldsymbol{\ell}_1) \hat{I}_{\gamma, \text{sm}}^*(\boldsymbol{\ell}_2) \rangle, \\ &= \int \frac{d^2\ell_1}{(2\pi)^2} e^{i\ell_1 \cdot \boldsymbol{\theta}_{12}} C^{\kappa I_\gamma}(\ell_1) \\ &\quad \times \hat{W}(\ell_1, \theta_G) \hat{U}_\kappa(\ell_1, \theta_G), \end{aligned} \quad (22)$$

where characters with hats represent quantities in Fourier space,  $\delta^{(2)}(\mathbf{x})$  is the dirac delta function in two-dimensional space,  $\boldsymbol{\theta}_{12} = \boldsymbol{\theta}_1 - \boldsymbol{\theta}_2$ , and we define the cross power spectrum  $C^{\kappa I_\gamma}$  as,

$$\langle \hat{\kappa}(\boldsymbol{\ell}_1) \hat{I}_\gamma(\boldsymbol{\ell}_2) \rangle \equiv C^{\kappa I_\gamma}(\ell_1) (2\pi)^2 \delta^{(2)}(\boldsymbol{\ell}_1 - \boldsymbol{\ell}_2). \quad (23)$$

Here we use the relations of Eqs. (18) and (21) in Fourier space,

$$\hat{\kappa}_{\text{sm}}(\boldsymbol{\ell}) = \hat{U}_\kappa(\ell, \theta_G) \hat{\kappa}(\boldsymbol{\ell}), \quad (24)$$

<sup>2</sup> We chose the number of mock catalogs so that the inverse covariance matrix in our analysis has a  $\sim 10\%$  accuracy. Ref. [44] examine the bias in estimating the inverse covariance matrix as a function of independent random realizations. They find that the amplitude of bias depends on the ratio of the number of bins (data vector variables) to the number of data sets. There are 16 data variables in our cross correlation analysis. With 200 random realizations, we expect that the bias in the inverse covariance matrix is as small as  $200/(200 - 16 - 1) \simeq 1.09$ .

Name of patch	$n_{\text{gal}}$ (No selection in $z_{\text{photo}}$ )	$n_{\text{gal}}$ ( $0.3 < z_{\text{photo}} < 0.8$ )	$n_{\text{gal}}$ ( $0.8 < z_{\text{photo}} < 1.2$ )	$n_{\text{gal}}$ ( $1.2 < z_{\text{photo}} < 1.9$ )	Effective area ( $\text{deg}^2$ )
GAMA09H	16.8	7.93	3.84	2.72	21.53
GAMA15H	21.5	9.32	5.29	3.85	38.04
HECTOMAP	18.1	8.10	4.65	3.04	18.78
VVDS	19.2	8.30	4.71	3.56	24.49
WIDE12H	23.0	10.1	5.91	4.13	16.16
XMM	19.9	8.61	5.12	3.57	34.52

TABLE I. Summary of lensing data used in this paper.  $n_{\text{gal}}$  represents the weighted number density of source galaxies in unit of  $\text{arcmin}^{-2}$ , and the last column shows the effective survey area. The effective survey area is defined by the unmasked pixels in our EGB and convergence maps. The definition of mask in our analysis is found in Section III B.

$$\hat{I}_{\gamma, \text{sm}}(\ell) = \hat{W}(\ell, \theta_G) \hat{I}_{\gamma}(\ell), \quad (25)$$

where  $W$  and  $U_{\kappa}$  are defined as Eqs. (17) and (19), respectively. For a given filter of  $f(\theta)$ , its Fourier counterpart is written as,

$$\hat{f}(\ell) = \int_0^{\infty} 2\pi\theta d\theta f(\theta) J_0(\ell\theta), \quad (26)$$

where  $J_0(x)$  is the zero-th Bessel function. Hence, we can obtain the expectation value of Eq. (20) by setting  $\theta_{12} = 0$  in the right-hand side of Eq. (22).

The cross power spectrum  $C^{\kappa I_{\gamma}}$  can be expressed as [14, 15, 25],

$$C^{\kappa I_{\gamma}}(\ell) = \sum_X \int \frac{d\chi}{r^2(\chi)} W_{g,X}(\chi) W_{\kappa}(\chi) \times P_{mg,X} \left( \frac{\ell + 1/2}{r(\chi)}, z(\chi) \right), \quad (27)$$

where  $P_{mg,X}$  represents the three-dimensional cross power spectrum between the matter density and the number density of astrophysical source population  $X$  in the EGB. Here we ignore possible contributions from intrinsically diffuse processes such as dark-matter annihilation and decay<sup>3</sup>. We also note that the effect of the energy dependent  $\gamma$ -ray PSF is properly included as in Ref. [22], when we compare our model with the observed cross correlations.

Before going to the detailed computation, we describe our smoothing filters in Fourier space and the window function along a line of sight. Figure 2 shows the effective smoothing filter  $\hat{W}\hat{U}_{\kappa}$  in Eq. (22). According to this figure, our filters in Eqs. (17) and (19) can be regarded as high-pass and low-pass in smoothing. In the range of  $\theta_G = 30 - 60$  arcmin, we can efficiently extract the information of clustering signature between Fourier modes with narrow range of  $\ell \sim 100$ . Furthermore, Figure 3 summarizes the relevant window functions along a line of sight in our analysis. Because of the nature of gravitational lensing, we can effectively remove the contribution

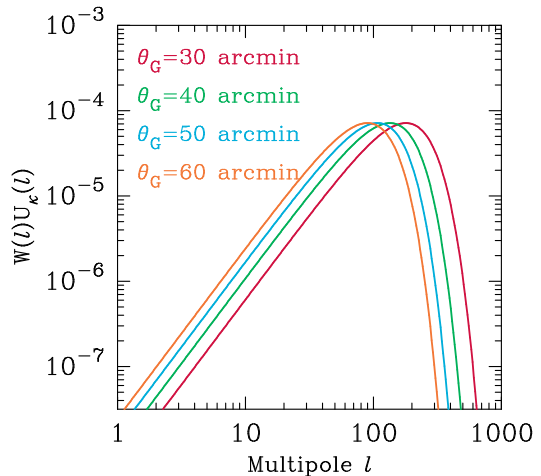


FIG. 2. Effective smoothing filter in our cross-correlation analysis. The horizontal axis shows the product of two filters of interest in Fourier space. The difference in colors represent the case with different smoothing scales  $\theta_G$ . Over the range of  $\theta_G \sim 30$  to 60 arcmin, our filter effectively extracts information of  $\ell \sim 100$ , i.e., clustering in degree scales.

from very low-redshift structures. The effective window function in the computation of  $C^{\kappa I_{\gamma}}$  is broad in redshift, but we can find that the effective redshift will be of the order of  $\sim 0.5$  corresponding to  $\chi \sim 1$  Gpc. Therefore, the main contribution in Eq. (27) will come from the clustering between matter density and  $\gamma$ -ray sources at  $\sim 10$  Mpc, where the linear theory in structure formation is valid with reasonable accuracy.

## B. A model of bias of astrophysical sources

We introduce our fiducial model of astrophysical sources. Our model is largely based on the one developed in Ref. [25]. This model is found to be consistent with the observed cross correlation signals between the IGRB and the gravitational-lensing effect in the CMB [20]. As seen above, the expected correlation can be mostly set by the linear part of the clustering. In this case, the three-dimensional cross power spectrum can be approximated as  $P_{mg,X}(k, z) = b_{\text{eff},X}(z) P_L(k, z)$ , where  $P_L(k, z)$  is the linear matter power spectrum at redshift  $z$  and  $b_{\text{eff},X}$  is

<sup>3</sup> Cosmological constraints of dark-matter annihilation with our measurements are provided in the Appendix, while our method seems more suitable for studying astrophysical contributions in the EGB.



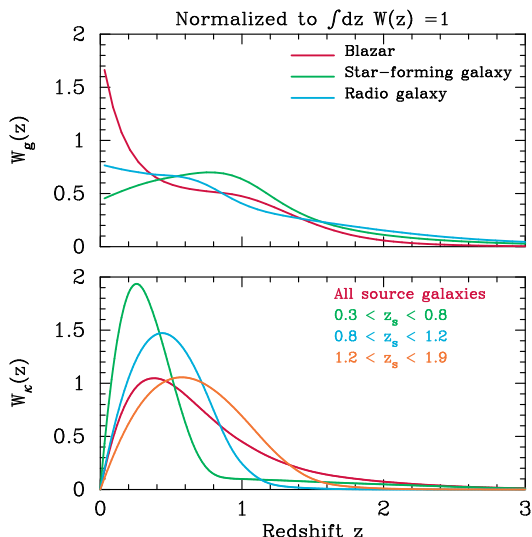


FIG. 3. Window function in redshift direction. Upper panel represents the window for EGB and different colored lines show the window for different astrophysical sources. We work with the  $\gamma$ -ray energy range of 1–500 GeV. The bottom panel is the window for lensing convergence. Here, we consider the four cases with different source-galaxy redshift selections in the HSC16A data: no selections (red),  $0.3 < z_{\text{photo}} < 0.8$  (green),  $0.8 < z_{\text{photo}} < 1.2$  (cyan), and  $1.2 < z_{\text{photo}} < 1.9$  (orange). Note that every window function is normalized to  $\int dz W(z) = 1$ .

the effective bias for source population  $X$ . We follow the standard halo-model approach to evaluate  $b_{\text{eff},X}$  [14, 25]. Assuming correlation between the  $\gamma$ -ray luminosity and host halo mass  $M_h$  of  $\gamma$ -ray source, one can find,

$$b_{\text{eff},X}(z) = \frac{\int dL_\gamma b_h(M_{h,X}(L_\gamma, z)) L_\gamma \Phi_X(L_\gamma, z)}{\int dL_\gamma L_\gamma \Phi_X(L_\gamma, z)} \quad (28)$$

where  $\Phi_X$  is the luminosity function of the source population  $X$  (here we already perform the integral over the photon index  $\Gamma_X$  if needed),  $M_{h,X}(L_\gamma, z)$  represents the relation of host halo and the  $\gamma$ -ray luminosity, and  $b_h$  is the linear halo bias. In this paper, we adopt the model of  $b_h$  in Ref. [47].

For blazars, we use the model in Ref. [48], which has introduced a simple power-law scaling  $M_h = A(z) \mathcal{L}_{X-\text{ray}}^{B(z)}$ , to the X-ray luminosity  $\mathcal{L}_{X-\text{ray}}$  so that the model can reproduce well the abundance of X-ray selected AGNs at different redshifts (see their Fig. 6 and Table 1). To relate the X-ray luminosity to the  $\gamma$ -ray luminosity, we introduce the relation between the bolometric blazar luminosity  $P$  and disk X-ray luminosity as  $P = 10^q \mathcal{L}_{X-\text{ray}}$  [49]. The parameter  $q$  is set to be 4.21 as follows in Ref. [7].

For star-forming and radio galaxies, constructing the possible relation between  $M_h$  and  $L_\gamma$  is more uncertain since there exists limited data. In the case of star-forming galaxy, we adopt the benchmark model in Refs. [14, 25]  $M_h = 10^{12} M_\odot (L_\gamma / 10^{39} \text{ erg s}^{-1})^{1/2}$ , where it is evaluated

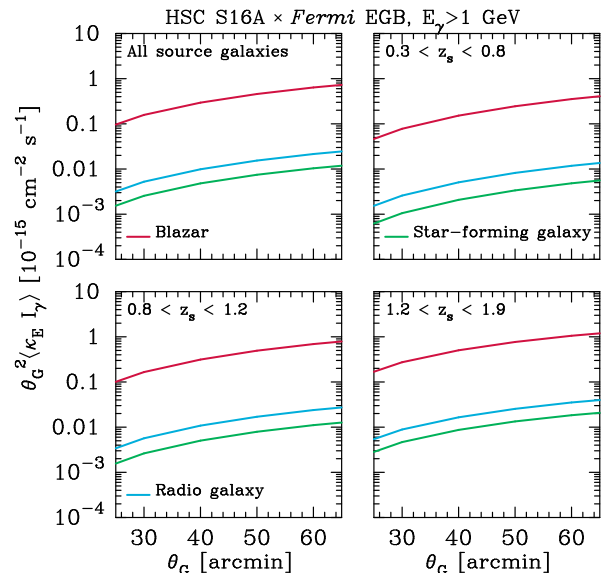


FIG. 4. Expected cross correlation signal between the EGB and lensing convergence. Each panel shows the results using different source galaxies selected by their photometric redshift in the lensing analysis. In each panel, the red line represents the contribution from correlation to blazars, the green is for star-forming galaxy and the cyan is for radio galaxy. The blazar contribution is expected to be dominant, indicating that we can constrain the physical property of blazars with our cross correlation analysis.

with reasonable approximation that the mass associated to the maximum luminosity will not exceed a maximum galactic mass. Ref. [25] also constructed a model for the  $M_h - L_\gamma$  relation for radio galaxies by using data from 12 available AGNs and possible relation in mass between dark-matter halo and super-massive black hole (SMBH) [48, 50]. The best-fit relation can be approximated as  $M_h = 3.2 \times 10^{12} M_\odot (L_\gamma / 10^{41} \text{ erg s}^{-1})^{0.11}$ . Although one can construct more physical models, such as examined in Ref. [25], we expect that our main results will be weakly sensitive to the choice of the  $M_h - L_\gamma$  relation for star-forming and radio galaxies. This is because the dominant contribution to the EGB is expected to be from blazars, and the window function for blazars is much larger than that of other contributions at redshifts relevant in our analysis. Note that the window function in EGB  $W_{g,X}$  is now constrained by the measurement of the EGB energy spectrum [4, 12] and it seems difficult to increase the contribution from star-forming and radio galaxies furthermore in the range of 1-500 GeV.

Figure 4 shows the expected signal from our fiducial model of astrophysical  $\gamma$ -ray sources. The figure clearly demonstrates that the blazar population gives a much larger contribution to  $\langle \kappa_E I_\gamma \rangle$  than the others. The difference can be a factor of 10 – 100 in our lensing analysis. These results strongly motivate us to constrain the physical properties of blazars with our cross correlation analysis. We emphasize that the expected signal



Tomographic bins	$\langle \kappa_E I_\gamma \rangle$	$\langle \kappa_B I_\gamma \rangle$
No selection in $z_{\text{photo}}$	1.84 (4)	1.07 (4)
$0.3 < z_{\text{photo}} < 0.8$	0.82 (4)	1.14 (4)
$0.8 < z_{\text{photo}} < 1.2$	1.96 (4)	3.92 (4)
$1.2 < z_{\text{photo}} < 1.9$	4.31 (4)	0.61 (4)
Combined	7.41 (16)	8.95 (16)

TABLE II. Summary of the significance of our cross-correlation measurements. Second and third columns represent the  $\chi_0^2$  defined in Eq. (29) and the numbers in brackets show the degree of freedom in the analysis. Note that we take into account the off-diagonal terms in the covariance between different smoothing scales and source-galaxy redshift selections.

is largely contributed by the structures at  $z \sim 0.5$ , because the cross correlation is proportional to the factor of  $W_{g,X} \times W_\kappa$  (also see Figure 3 and Eq. [27]). Hence, the correlation can be used to probe the clustering of blazars at relatively high redshift, which is inaccessible through auto-correlation of the resolved blazars.

## V. RESULT

### A. Cross correlation

Figure 5 summarizes our cross-correlation measurements. The error bars in this Figure are evaluated with 200 mock catalogs of galaxy shapes in HSCS16A. The results of using different galactic  $\gamma$ -ray templates to construct the EGB (see appendix A for details) are shown by different colors. We confirm that the systematic uncertainty due to imperfect knowledge of galactic  $\gamma$ -ray components is smaller than the current statistical uncertainty. This is because the ROI in the HSCS16A is sufficiently far from the Galactic plane and the galactic  $\gamma$ -ray contribution from  $\pi^0$  decays can be well constrained. Similar results have been found in Ref. [23]. In addition, we also examine the cross correlation with the B-mode convergence  $\kappa_B$  which is commonly used as an indicator of systematic uncertainties in the galaxy-shape measurement. The bottom set of 4 panels in Figure 5 show the cross correlation with  $\kappa_B$ . We define the significance of our measurements, i.e., null signals, as

$$\chi_0^2 = \sum_{s,s'} \sum_{i,j} \mathbf{C}_{ij}^{-1}(s,s') \times \langle \kappa_E I_\gamma \rangle(\theta_{G,i}; s) \langle \kappa_E I_\gamma \rangle(\theta_{G,j}; s'), \quad (29)$$

where  $\langle \kappa_E I_\gamma \rangle(\theta_{G,i}; s)$  represents the cross correlation for smoothing scale  $\theta_{G,i}$  with source galaxy selection  $s$ , and  $\mathbf{C}(s,s')$  is the covariance estimated from 200 mock catalogs. We find that the cross correlation is consistent with null detection in all cases. Table II summarizes the  $\chi_0^2$  in our measurements.

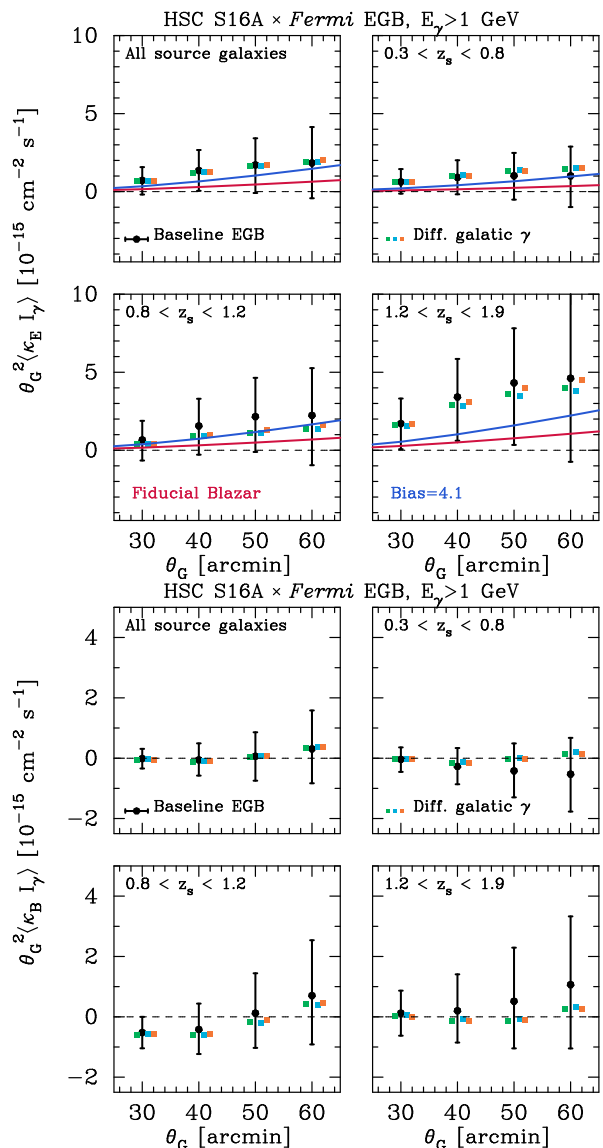


FIG. 5. We plot the cross-correlations between FermiLAT and HSCS16A data. *Top*: The lensing convergence  $\kappa_E$  - EGB correlation as defined in Eq. (20). The four panels show the results obtained from different source-galaxy selections by source redshift  $z_{\text{photo}}$ : all source galaxies (top left),  $0.3 < z_{\text{photo}} < 0.8$  (top right),  $0.8 < z_{\text{photo}} < 1.2$  (bottom left), and  $1.2 < z_{\text{photo}} < 1.9$  (bottom right). The black points with error bars show the measurement using our baseline EGB maps, while the colored points with small offsets represent the cases with different galactic  $\gamma$ -ray templates used to construct the EGB (see appendix A for details). Red lines correspond to our fiducial model of blazar clustering (see Section IV B for details). Blue lines show the expected correlation signal with a constant blazar bias of 4.1. This large bias is found to be consistent with stacked analysis of  $\kappa_E$  around resolved point sources (see Section V C for details). *Bottom*: As above, but for the B-mode convergence  $\kappa_B$ , which is equivalent to the imaginary part in Eq. (13). The small correlation between the EGB and  $\kappa_B$  suggests that the galaxy shape measurement is accurate enough. Note that each data point should be correlated with each other.

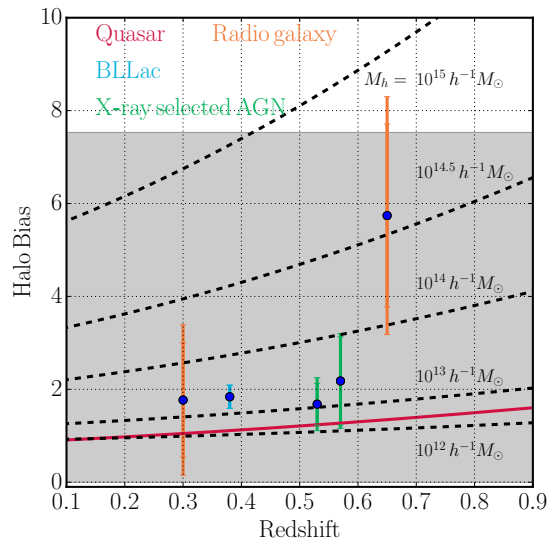


FIG. 6. Allowed blazar bias (gray shaded region) compared with other clustering measurements of AGNs at different wavelengths. The red line shows the bias of quasars obtained from the 2dF QSO Redshift survey [51], the green data points are for the bias measurement of X-ray selected AGNs in the XMM Cosmic Evolution Survey [52], the cyan data point represents the bias measurement of resolved blazars in the 2-year all-sky survey by Fermi-LAT [16], and the orange data point is for the bias measurement of radio galaxies in the Very Large Array Faint Images of the Radio Sky at Twenty-cm survey (FIRST) [53]. For reference, the dashed line shows the linear halo bias with a fixed mass [47].

## B. Implications for blazar-halo connection

Since weak gravitational lensing provides a direct, physical probe of the cosmic matter density distribution, our cross-correlation measurement can be used to determine or constrain the clustering bias of  $\gamma$ -ray sources with respect to the underlying density field. The top panels of figure 5 compare the observational data with our fiducial model predictions for the cross correlation expected from blazars (red lines). Interestingly, the data suggest even stronger clustering than our fiducial model predicts. Our model of blazar clustering (Section IV B) predicts a bias factor  $b_{\text{eff}} \simeq 2$  over the redshift range of interest, which is consistent with the recent measurement of the blazar auto-correlation [16]. Although the statistical errors are still large, our cross-correlation analysis suggests that the EGB sources may be a more biased tracer of the large-scale structure than expected.

We can use the cross-correlation to place constraints on the blazar bias. Assuming the observed data follow multivariate Gaussian with covariance matrix  $\mathbf{C}$ , we introduce the  $\chi^2$  statistics,

$$\chi^2 = \sum_{s,s'} \sum_{i,j} \mathbf{C}_{ij}^{-1}(s,s') \{ \langle \kappa_E I_\gamma \rangle(\theta_{G,i}; s) - \mu_{i,s}(\mathbf{p}) \}$$

$$\times \{ \langle \kappa_E I_\gamma \rangle(\theta_{G,j}; s') - \mu_{j,s'}(\mathbf{p}) \}, \quad (30)$$

where  $\mu_{i,s}$  represents theoretical template of interest for observed  $\langle \kappa_E I_\gamma \rangle(\theta_{G,i}; s)$ . In our theoretical model, we assume a constant blazar bias over redshift, i.e.,  $b_{\text{eff}}(z) = \text{const}$ , for simplicity. The data consist of four bins in  $\theta_G$  with four different source-galaxy selections in the lensing analysis. Hence, we have  $4 \times 4 = 16$  degrees of freedom, whereas there is only a single parameter in our model. The constraint on the parameter can be obtained by  $\chi^2 - \chi_0^2 < 1$ , corresponding to a 68% confidence level. Using our measurements, we derive an upper limit on the blazar bias of  $b_{\text{eff}} < 7.53$ . We show the constraint in figure 6 as the gray shaded region, and compare it with the bias measurements of AGNs selected at different wavelengths. The overall uncertainty remains fairly large, both in the bias parameter and in the source redshift, but it is intriguing that blazars contributing to the EGB may likely reside in massive dark halos at  $z \sim 0.3 - 0.7$ .

## C. Stacked convergence profile around resolved $\gamma$ -ray sources

As a cross-check of our findings, we also study the lensing signals around *resolved*  $\gamma$ -ray sources in the HSCS16A fields.

### Estimator

We stack the reconstructed convergence  $\kappa_E$  from galaxy shapes in HSCS16A, and calculate the  $\kappa_E$  profile around the resolved  $\gamma$ -ray sources. The estimator of the stacked profile is given by

$$\langle \kappa_E \rangle(\theta) = \frac{\sum_{i,j} w_{ij} n_\gamma(\phi_i) \kappa_E(\phi_j)}{\sum_{i,j} w_{ij} n_\gamma(\phi_i)} - \frac{\sum_{i,j} w_{ij} n_{\text{rand}}(\phi_i) \kappa_E(\phi_j)}{\sum_{i,j} w_{ij} n_{\text{rand}}(\phi_i)}, \quad (31)$$

where  $n_\gamma$  represents the number density field of  $\gamma$ -ray sources and  $n_{\text{rand}}$  is the number density field of random points. In Eq. (31), we set the linear angular binning with a bin width  $\Delta\theta$  so as to be  $w_{ij} = 1$  if  $\theta - \Delta\theta/2 < |\phi_i - \phi_j| < \theta + \Delta\theta/2$  and  $w_{ij} = 0$  otherwise. The stacked profile of B-mode convergence  $\langle \kappa_B \rangle$  can be estimated similarly to Eq. (31). Note that  $\langle \kappa_B \rangle$  should vanish if there are no systematic effects in galaxy shape measurements.

### Expectation value

The expectation value of Eq. (31) is computed as

$$\langle \kappa_E \rangle(\theta) = \int \frac{d^2\ell}{(2\pi)^2} e^{i\ell \cdot \theta} C^{\kappa n_\gamma}(\ell) \hat{U}_\kappa(\ell, \theta_G), \quad (32)$$

where  $\hat{U}_\kappa$  is the Fourier counterpart of Eq. (19). We here define the cross power spectrum between lensing convergence and the photon number density fluctuation field as

$$\langle \hat{\kappa}(\ell_1) \hat{\delta}_\gamma(\ell_2) \rangle \equiv C^{\kappa n_\gamma}(\ell_1) (2\pi)^2 \delta^{(2)}(\ell_1 - \ell_2), \quad (33)$$

where  $\delta_\gamma = n_\gamma / \bar{n}_\gamma - 1$  and  $\bar{n}_\gamma$  is the average angular number density of  $\gamma$ -ray sources. Under the linear approximation, we express the cross power spectra as

$$C^{\kappa n_\gamma}(\ell) = \int \frac{d\chi}{r^2(\chi)} W_{\text{ps}}(\chi) W_\kappa(\chi) \times b_{\text{ps}}(z) P_L \left( k_\ell = \frac{\ell + 1/2}{r(\chi)}, z(\chi) \right), \quad (34)$$

$$W_{\text{ps}} = \mathcal{C} \chi^2 \int_{L_{\text{min}}(z)} dL_\gamma \Phi_{\text{ps}}(L_\gamma, z), \quad (35)$$

where  $\Phi_{\text{ps}}(L_\gamma, z)$  is the luminosity function of point sources and the window function  $W_{\text{ps}}$  is normalized to  $\int d\chi W_{\text{ps}} = 1$ . We simply assume that all the resolved sources in our ROIs are blazars. The lower limit in the integral in Eq. (35) is given by the flux limit in the  $\gamma$ -ray observations. To compute  $L_{\text{min}}$ , we assume the  $\gamma$ -ray energy spectrum of blazars (see Eq. 7) and set the flux limit to be  $2 \times 10^{-9} \text{ cm}^{-2} \text{ s}^{-1}$  above 100 MeV.

### Result

Figure 7 shows the stacked convergence profile around resolved  $\gamma$ -ray sources. We reconstruct the lensing convergence with a Gaussian smoothing scale of 60 arcmin; the large smoothing scale assures that our measurements are insensitive to non-linear clustering of point sources. To select the background source galaxies robustly in the lensing analysis, and to reduce the possible contamination by high- $z$   $\gamma$ -ray sources, we select the HSC galaxies by photometric redshifts to be in the range of  $1.2 < z_{\text{photo}} < 1.9$ . We also use only  $\gamma$ -ray point sources at  $z < 1$ . After the redshift selection, we find 118  $\gamma$ -ray sources available for our analysis. When performing the stack analysis, we set the angular bin width to be  $\Delta\theta = 0.1$  deg. The number of random points is set to be 100 times as large as the number of point sources. To estimate the statistical uncertainty, we utilize 200 mock HSC catalogs.

The bottom panel in figure 7 shows non-zero B-mode convergence at large angular scales of  $\theta > 0.6$  deg. It indicates that the current data do not allow us to derive  $\langle \kappa_E \rangle$  accurately, and thus we simply ignore the large-scale signals in the following discussions. Similarly to the method in Section V A, we compute the detection significance of the stacked convergence profile (also see Eq. 29). We find that  $\chi_0^2 = 3.75$  for  $\langle \kappa_E \rangle$  and 2.89 for  $\langle \kappa_B \rangle$  with 6 degrees of freedom. Hence, the current measured signal is still

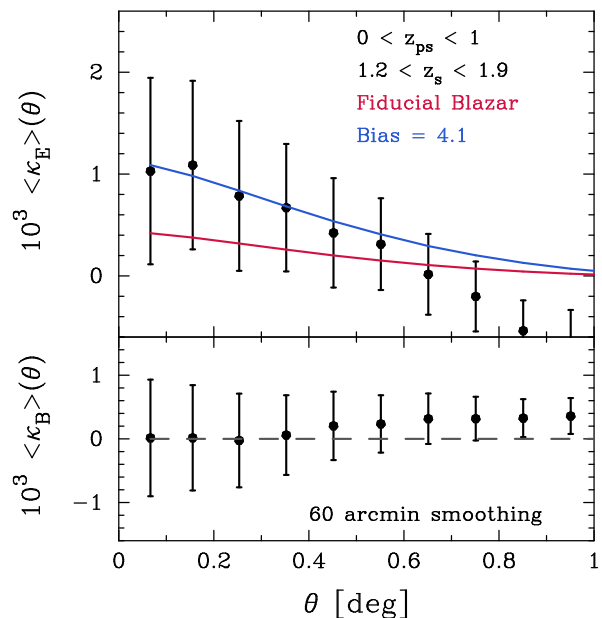


FIG. 7. The measurement of the average convergence profile around  $\gamma$ -ray point sources in the HSC16A fields. The upper panel shows the stacked profile of lensing convergence  $\langle \kappa_E \rangle$  as a function of separation angle from a point source,  $\theta$ . To reconstruct  $\kappa_E$  from galaxy shapes, we impose a photometric redshift selection of  $1.2 < z_{\text{photo}} < 1.9$  and set a Gaussian smoothing scale of 60 arcmin. To increase the detectability of lensing effects, we also consider foreground  $\gamma$ -ray sources by using their redshifts  $z_{\text{ps}}$  smaller than 1. In the upper panel, the red line shows the expected convergence profile from our fiducial model of blazar clustering, while the blue line is for a simple model with a large blazar bias of 4.1. Note that a bias of 4.1 provides the minimum chi-squared value for  $\langle \kappa_E \rangle$  at  $\theta < 0.6$  deg. The lower panel plots the B-mode convergence  $\langle \kappa_B \rangle$ , which is expected to be zero in the absence of significant systematic effects in the lensing survey. As shown in the lower panel, we find a non-zero  $\kappa_B$  at  $\theta \gtrsim 0.6$  deg, indicating the large-scale  $\kappa_E$  signals are not reliable for quantitative analyses.

consistent with null detection<sup>4</sup>. Although the statistical errors are large, we find that  $b_{\text{ps}} = 4.1$  in Eq. (34) provides a reasonable fit to the observed  $\langle \kappa_E \rangle$ , as shown by the solid line in the Figure. Similarly to our finding in Section V B, we observe that the stacked lensing analysis also implies a large bias of blazars in our ROIs.

<sup>4</sup> We have also confirmed that the stacked signal is still consistent with a null detection when setting the smoothing scale to 30 arcmin. In this case, the detection significance is found to be  $\chi_0^2 = 6.03$  for  $\langle \kappa_E \rangle$  and 3.19 for  $\langle \kappa_B \rangle$  with 6 degrees of freedom. At face value, a bias of  $\sim 4.8$  can provide a reasonable fit to the observed  $\langle \kappa_E \rangle$  in this case.

## VI. CONCLUSION AND DISCUSSION

In this paper, we have calculated the cross correlation of the EGB (i.e., the whole extragalactic  $\gamma$ -ray radiation including resolved sources) and the cosmic matter density at  $z \lesssim 1$  for the first time. One may naively expect a strong correlation between the two if the EGB is mostly contributed by known astrophysical sources [12]. The cross correlation at degree angular scales is found to be consistent with a null detection given the current statistical uncertainties. The result still allows us to constrain possible relations between the dominant source population of the EGB and the underlying mass distribution. We have tested and confirmed that our measurement is robust in terms of residual systematic effects in both the  $\gamma$ -ray and lensing analyses.

Provided that the astrophysical models in Section II A can reproduce the observed EGB spectrum well, we argue that the correlation of blazars and the large-scale matter density dominates the measured cross correlation at degree scales. This allows us to derive an estimate of the blazar bias with respect to the underlying matter density at  $z \sim 0.5$ . The clustering bias can be used to infer the host environment of the blazar population in the hierarchical structure formation model, and also to examine the unified AGN scenario [54]. Although our cross-correlation measurements are still consistent with a null detection, we find that a large bias of  $\sim 4$  provides a reasonable explanation for the EGB-lensing correlations. The blazar bias of  $\sim 4$  is also favored in order to explain the stacked lensing convergence profile around the resolved  $\gamma$ -ray sources. Our measurements allow to constrain a constant blazar bias. Interestingly, our result is consistent with other observations of AGN bias selected at different wavelengths (Figure 6).

The HSC final data with a sky coverage of 1,400 squared degrees will allow us to measure the clustering bias of blazars more accurately. Assuming that the statistical uncertainty of the cross-correlation is reduced with survey area, we should be able to detect the correlation between blazars and the matter density at a  $\sim 3\sigma$  level if the  $\gamma$ -ray sources are strongly clustered as indicated in the present paper. The cross correlation of the EGB and the HSC final data will offer invaluable information on the sources that give a dominant contribution to the EGB at  $z > 0.5$ , and provide a stringent statistical test of the unified AGN scenario at  $\gamma$ -ray energy scales. If the blazar bias is determined accurately, one can develop realistic models of the blazar population in the context of structure formation in a similar manner to that applied to SDSS galaxies [55].

Identifying the sources of the EGB remains a major goal for gamma-ray astrophysics. We need multiple information to reveal possible contributions from star-forming galaxies, radio galaxies, and diffuse processes. Joint measurements of multiple cross-correlation functions will be the key to this end. It is suggested that the cross-correlation of local galaxies and the cosmic infrared back-

ground helps to infer the star-forming activity in galaxies over a wider range of redshifts [17, 56, 57], while observations of galaxy clusters, radio galaxies, and the CMB lensing effect will tighten the constraints on the contribution from misaligned AGN [18, 20]. Furthermore, a tomographic approach using  $\gamma$ -ray energies and redshifts of LSS tracers will be viable with upcoming galaxy surveys [25, 58]. Ultimately, by putting all these information together, we will be able to understand the contributions to the EGB and perform stringent searches on the particle nature of dark matter. This *cosmological* probe will be highly complementary to searches using  $\gamma$ -ray measurements of local galaxies [59, 60].

## ACKNOWLEDGMENTS

The authors thank an anonymous referee for careful reading and suggestion to improve the article. We also thank Yutaka Komiyama for providing useful comments on the manuscript. The work of SH is supported by the U.S. Department of Energy under award number de-sc0018327. NY acknowledges financial support from JST CREST (JPMJCR1414). Numerical computations presented in this paper were in part carried out on the general-purpose PC farm at Center for Computational Astrophysics, CfCA, of National Astronomical Observatory of Japan.

The Hyper Suprime-Cam (HSC) collaboration includes the astronomical communities of Japan and Taiwan, and Princeton University. The HSC instrumentation and software were developed by the National Astronomical Observatory of Japan (NAOJ), the Kavli Institute for the Physics and Mathematics of the Universe (Kavli IPMU), the University of Tokyo, the High Energy Accelerator Research Organization (KEK), the Academia Sinica Institute for Astronomy and Astrophysics in Taiwan (ASIAA), and Princeton University. Funding was contributed by the FIRST program from Japanese Cabinet Office, the Ministry of Education, Culture, Sports, Science and Technology (MEXT), the Japan Society for the Promotion of Science (JSPS), Japan Science and Technology Agency (JST), the Toray Science Foundation, NAOJ, Kavli IPMU, KEK, ASIAA, and Princeton University.

The Pan-STARRS1 Surveys (PS1) have been made possible through contributions of the Institute for Astronomy, the University of Hawaii, the Pan-STARRS Project Office, the Max-Planck Society and its participating institutes, the Max Planck Institute for Astronomy, Heidelberg and the Max Planck Institute for Extraterrestrial Physics, Garching, The Johns Hopkins University, Durham University, the University of Edinburgh, Queen's University Belfast, the Harvard-Smithsonian Center for Astrophysics, the Las Cumbres Observatory Global Telescope Network Incorporated, the National Central University of Taiwan, the Space Telescope Science Institute, the National Aeronautics and Space Ad-

ministration under Grant No. NNX08AR22G issued through the Planetary Science Division of the NASA Science Mission Directorate, the National Science Foundation under Grant No. AST-1238877, the University of Maryland, and Eotvos Lorand University (ELTE).

This paper makes use of software developed for the Large Synoptic Survey Telescope. We thank the LSST Project for making their code available as free software at <http://dm.lsst.org>.

Based [in part] on data collected at the Subaru Telescope and retrieved from the HSC data archive system, which is operated by the Subaru Telescope and Astronomy Data Center at National Astronomical Observatory of Japan.

## Appendix A: FERMI-LAT ANALYSIS METHODS

The analysis of the full  $20^\circ \times 20^\circ$  *Fermi*-LAT data sets encompassing each of the HSC regions was divided into four smaller regions, each of which was modeled by a diffuse  $\gamma$ -ray background and  $\gamma$ -ray point source model. Namely, we divided each  $20^\circ \times 20^\circ$  region into four  $12^\circ \times 12^\circ$  contiguous patches with overlapping boundaries for which we started the fit with a sky model that includes all point-like and extended LAT sources listed in the 3FGL [61] catalog as well as with models for the Galactic diffuse and isotropic emission. In our baseline model the Galactic diffuse emission was modeled by the standard LAT diffuse emission model `gll_iem_v06.fits`, and as a proxy for the residual background and extragalactic  $\gamma$ -ray radiation spectra we used a single isotropic component with the spectral shape given by model `iso_P8R2_ULTRACLEANVETO_V6_v06.txt`<sup>5</sup>.

We used the *Fermipy* Python package<sup>6</sup> in conjunction with standard *Fermi Science Tools* to fit and characterize the sources included in the sky models corresponding to each region of interest (ROI). In each ROI we bin the LAT data in 8 energy bins per decade and with a spatial pixel size of  $0.1^\circ$ . Each ROI is analyzed separately; however, in order to perform our cross correlation analysis in the full HSC regions we merge the patches from the analyses of the different ROIs.

Using the initial baseline model mentioned above, the first step of our method is to find the best spectral parameters for all free sources within our  $12^\circ \times 12^\circ$  ROIs. To obtain convergence, all the fits were performed hierarchically; freeing first the normalization of the sources with the highest intensities followed by the lower ones within the ROIs. The fitting consecutively restarts from the updated best-fit models and repeats the same procedure this time for the spectral shape parameters. Due to the  $\sim 7$  years of LAT data used in our analysis compared

to the 4 years of the 3FGL [61] catalog, we expected to find new  $\gamma$ -ray point source candidates in our ROIs. The significance of each new point source candidate was evaluated using the test statistic  $TS = 2(\ln \mathcal{L}_1 - \ln \mathcal{L}_0)$ , where  $\mathcal{L}_0$  and  $\mathcal{L}_1$  are the likelihoods of the background (null hypothesis) and the hypothesis being tested (alternative hypothesis: background plus source). All point source candidates that were found to have a  $TS \geq 25$  were included to our sky model of the respective ROI. The new *Fermipy* package includes special routines to perform automated point source searches, and in this study we followed the standard method recommended in the *Fermipy* documentation. We then used this package to refine the positions and the spectral parameters of the new point source candidates. Since the set of four  $12^\circ \times 12^\circ$  patches making up every  $20^\circ \times 20^\circ$  HSC ROI have some overlapping regions at the boundaries, we remove any duplicate point source candidates found in more than one patch. In this study we detected 48 new point source candidates with  $TS \geq 25$  in the combined the HSC ROIs. The positions and spatial overlaps with the Roma-BZCAT [62] Blazar catalog are shown in Table III. All the characteristics of the new point source candidates are provided in FITS files with this article.

The EGB photons in the ROIs were obtained by subtracting the best-fit Galactic diffuse emission model from the photon counts maps. We note that the EGB images obtained in this way could still contain some isotropic detector backgrounds. However, our analysis is able to reproduce well the EGB  $\gamma$ -rays derived by the *Fermi*-LAT team (see, e.g., Ref. [23] for an example of this method). This shows that most of the detector cosmic-ray induced backgrounds are safely removed by our conservative photon selection filters.

We estimated the systematic uncertainties in the Galactic diffuse emission model in a similar fashion to that explored in the Fermi collaboration paper on the EGB [4]. Namely, we reran our pipeline using the alternative foreground Models A, B and C as described in the appendix of Ref. [4]. Such foreground models encompass a very generous range of the systematics associated with this kind of analysis, and provides a test in rigor comparable to that performed by the *Fermi* team.

<sup>5</sup> <http://fermi.gsfc.nasa.gov/ssc/>

<sup>6</sup> <http://fermipy.readthedocs.io/en/latest/>.

TABLE III: New Point Source Candidates detected in the HSC ROIs.

Name	$l$ [deg]	$b$ [deg]	Association or spatial overlap	TS
PSJ0922.8+0432	227.74	35.48		44
PSJ0932.7+1040	222.40	40.57	5BZBJ0932+1042	28
PSJ0930.7+0031	233.24	35.02	5BZQJ0930+0034	76
PSJ0833.6-0455	229.77	20.07		35
PSJ0848.0-0704	233.77	21.97	5BZBJ0847-0703	101
PSJ0819.5-0755	230.58	15.53	5BZBJ0819-0756	36
PSJ1420.2+0612	352.20	60.28	5BZBJ1420+0614	37
PSJ1410.1+0202	343.20	58.62	5BZBJ1410+0203	139
PSJ1356.6+0237	338.22	60.92		48
PSJ1443.5-0959	342.98	43.99		34
PSJ1405.1-0642	333.41	51.74		30
PSJ1359.1-0658	331.03	52.17		29
PSJ1401.0-0914	330.23	49.90	5BZQJ1401-0916	61
PSJ1425.3-0119	345.15	53.66	5BZBJ1425-0118	33
PSJ1644.2+4544	71.33	40.84	5BZGJ1644+4546	42
PSJ1607.8+4947	77.85	46.40		36
PSJ1604.2+5008	78.59	46.91	5BZBJ1603+5009	54
PSJ1607.8+4950	77.90	46.39		42
PSJ1536.0+3744	60.58	54.02	5BZUJ1536+3742	253
PSJ1529.5+3813	61.70	55.23	5BZBJ1529+3812	29
PSJ1602.1+3328	53.77	48.71	5BZUJ1602+3326	33
PSJ2249.9+0451	75.76	-46.59		31
PSJ2226.5+0207	67.11	-44.48		28
PSJ2235.2-0631	59.21	-51.68		38
PSJ2301.0-0157	71.81	-53.49	5BZQJ2301-0158	136
PSJ2225.7-0803	55.01	-50.63		45
PSJ2156.1-0036	57.71	-40.32	5BZUJ2156-0037	127
PSJ2211.0-0004	61.32	-42.96	5BZBJ2211-0003	35
PSJ2148.0-0734	48.46	-42.42	5BZBJ2148-0733	80
PSJ1219.7+0446	282.89	66.39	5BZBJ1219+0446	47
PSJ1219.7+0547	282.00	67.39		37
PSJ1215.1+0734	277.57	68.63	5BZGJ1215+0732	53
PSJ1216.1+0931	276.01	70.52	5BZGJ1216+0929	58
PSJ1216.0-0243	285.59	58.96	5BZBJ1216-0243	36
PSJ1207.6-0104	280.65	59.89	5BZQJ1207-0106	69
PSJ1136.0-0426	270.09	53.55	5BZQJ1135-0428	45
PSJ1129.3-0530	268.53	51.82		59
PSJ1131.0-0945	272.35	48.29		45
PSJ0237.3+0206	168.27	-51.19		30
PSJ0239.8+0417	166.90	-49.10	5BZQJ0239+0416	95
PSJ0245.0-0257	176.18	-53.65		55
PSJ0208.6-0045	161.24	-57.79	5BZBJ0208-0047	38
PSJ0220.9-0841	176.01	-61.94	5BZBJ0220-0842	38
PSJ0226.6-0553	174.07	-58.96		63
PSJ0241.0-0506	177.65	-55.86	5BZBJ0240-0504	51
PSJ0205.8-0955	172.03	-65.42		33
PSJ0140.7-0758	156.59	-67.57	5BZBJ0140-0758	42
PSJ0142.6-0543	154.87	-65.36	5BZBJ0142-0544	35

New point source candidates in the HSC ROIs found with a  $TS \geq 25$  in  $\sim 7$  years of *Fermi*-LAT data. This table is also provided as a FITS file in the online material. The horizontal dividers separate the new point source candidates in the GAMA09H, GAMA15H, HECTOMAP, VVDS, WIDE12H and XMM patches, from top to bottom. The fourth column displays associations or spatial overlaps with tentative multi-wavelength counterparts. For this purpose we use the Roma-BZCAT blazar catalog [62]. To identify possible multi-wavelength counterparts to the new point source candidates we searched in the seed locations within the 68% containment of the point spread function for one of our high-energy bands, which comes to  $\sim 0.2^\circ$ .

## Appendix B: CROSS-CORRELATION WITH ISOTROPIC GAMMA-RAY COMPONENTS AND CONSTRAINTS ON DARK MATTER ANNIHILATION

In this appendix, we present the cross-correlation analysis of the lensing convergence and the isotropic  $\gamma$ -ray

background (IGRB) including the unresolved components in *Fermi*-LAT data.

The lensing convergence  $\kappa_E(\theta)$  is equivalent to the cos-



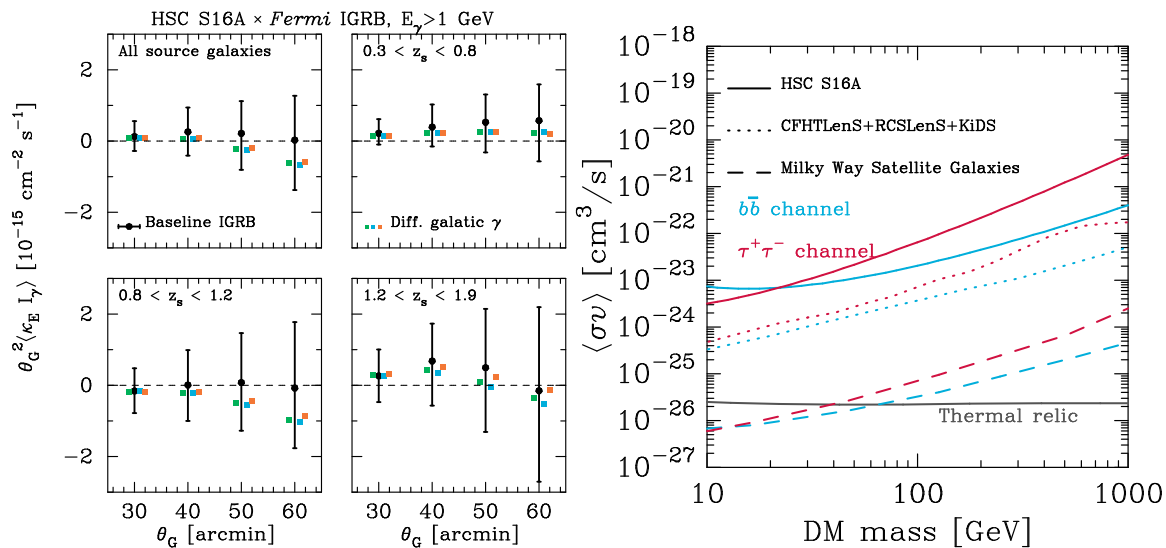


FIG. 8. *Left*: The cross-correlation of the IGRB and smoothed lensing convergence. Each panel shows the result obtained with different source-galaxy selections by photometric redshifts in the lensing analysis. The black points with error bars represent results with our baseline IGRB maps, while colored points are for the cases when we use different galactic  $\gamma$ -ray templates in the Fermi-LAT analysis pipeline. No significant correlations are found in all cases. Possible systematic effects by imperfect subtraction of galactic  $\gamma$  rays can be safely ignored in our analysis. *Right*: 95% confidence level upper limits on the DM annihilation cross section as a function of DM particle mass. The different colors correspond to two different annihilation channels ( $b\bar{b}$  and  $\tau^+\tau^-$ ). The solid lines present constraints from our cross correlation measurements using the HSCS16A data, while the dotted lines are for similar cross-correlation analysis with wider survey area coverage [24], and the dashed lines show the  $\gamma$ -ray emission constraints from local dwarf galaxies [60]. The gray line shows the canonical cross section expected for thermal relic DM [63].

mic surface mass density with a weight function along line-of-sight direction  $\theta$ . The details of the reconstruction algorithm of  $\kappa_E$  from the HSCS16A galaxy-imaging data are given in Section II B 2. We use the cross-correlation estimator in Eq. (20) to the IGRB measured by Fermi-LAT and the lensing convergence from HSCS16A. As in Section III C, we evaluate the statistical uncertainty of the cross correlation with 200 HSCS16A mock catalogs and use the inverse-weighted method to combine the cross-correlation signals for individual HSCS16A patches together. In addition to the normal masks as described in Section III C, we also place circular masks around Fermi-LAT  $\gamma$ -ray point sources, with a radius of 1 deg. The circular masks are introduced in order to minimize possible contaminants from residual  $\gamma$ -rays from resolved bright sources.

The left panels in Figure 8 summarize our cross correlation measurements of the IGRB and  $\kappa_E$ . We work with four different source-galaxy selections in the lensing analysis. Regardless of the choice of smoothing scales and galaxy selections, we find that the IGRB- $\kappa_E$  cross-correlation is consistent with a null detection. We also confirm that the cross-correlation measurements of the IGRB and the B-mode convergence is consistent with a null detection, suggesting that our lensing analysis is not compromised by systematic errors. Table IV summarizes the significance of our results using the definition in Eq. (29).

Tomographic bins	$\langle \kappa_E I_\gamma \rangle$	$\langle \kappa_B I_\gamma \rangle$
No selection in $z_{\text{photo}}$	1.24 (4)	5.50 (4)
$0.3 < z_{\text{photo}} < 0.8$	0.72 (4)	6.57 (4)
$0.8 < z_{\text{photo}} < 1.2$	1.13 (4)	5.87 (4)
$1.2 < z_{\text{photo}} < 1.9$	4.24 (4)	0.99 (4)
Combined	7.06 (16)	16.6 (16)

TABLE IV. Summary of the significance of our IGRB- $\kappa_E$  cross-correlation measurements. Second and third columns list the  $\chi_0^2$  values defined in Eq. (29), and the number with bracket shows the degree of freedom in the analysis.

We can derive constraints on dark matter (DM) annihilation directly using the cosmic matter density distributions. Using the formulation as described in Section IV A, we compute the expected correlation originating from DM annihilation. We adopt the model of cross power-spectrum between the matter density and  $\gamma$ -rays from DM annihilation as in Ref. [23] (see their Eq. [14]). We then consider a conservative model of substructures in DM halos [64]. Following a similar likelihood analysis as in Section V B, we can constrain the two parameters in DM annihilation, DM particle mass and the annihilation cross-section  $\langle \sigma v \rangle$ , for a given annihilation channel. The right panel in Figure 8 shows our cosmological constraints on DM annihilation. For comparison, we also present the constraints from similar analyses with shall-



lower but wider galaxy survey data [24], and from analyses of the Milky-Way satellite galaxies [60]. Since our measurements in the HSC16A cover a smaller sky area than Ref. [24], our constraints are found to be weaker. Also it is unlikely for us to be able to place constraint on DM annihilation at a similar level as the local measurements [60], even if we use the HSC final data release, because the increased sky coverage can improve the statistical uncertainty only by a factor of  $\sim 3 - 4$ .

There are two reasons why our analysis does not provide tight constraints on DM annihilation:

1. Our cross-correlation analysis uses linear-scale clustering alone (see Section IV A) that contains less information on the internal mass distribution of DM halos.

2. HSC is suited for measuring the matter distributions in the distant universe. The median source redshift in HSC is larger than those in other data in the literature. Cross-correlation of the IGRB with objects or the matter density at lower redshifts can be more optimal for indirect detection of DM annihilation (also see Ref. [65] for optimal targets in large-scale structure for indirect detection of DM annihilation).

Overall, the cross-correlation measurement presented in this paper is a more promising tool to explore expected correlations of astrophysical  $\gamma$ -ray sources with the cosmic matter density.

- 
- [1] W. L. Kraushaar, G. W. Clark, G. P. Garmire, R. Borke, P. Higbie, V. Leong, and T. Thorsos, *Astrophys. J.* **177**, 341 (1972).
- [2] F. Acero *et al.* (Fermi-LAT), *Astrophys. J. Suppl.* **218**, 23 (2015), arXiv:1501.02003 [astro-ph.HE].
- [3] P. Sreekumar *et al.* (EGRET Collaboration), *Astrophys. J.* **494**, 523 (1998), arXiv:astro-ph/9709257 [astro-ph].
- [4] M. Ackermann *et al.* (Fermi-LAT), *Astrophys. J.* **799**, 86 (2015), arXiv:1410.3696 [astro-ph.HE].
- [5] M. Fornasa and M. A. Sanchez-Conde, *Phys. Rept.* **598**, 1 (2015), arXiv:1502.02866 [astro-ph.CO].
- [6] *Astrophys. J.* **720**, 435 (2010), arXiv:1003.0895 [astro-ph.CO].
- [7] J. P. Harding and K. N. Abazajian, *JCAP* **1211**, 026 (2012), arXiv:1206.4734 [astro-ph.HE].
- [8] T. A. Thompson, E. Quataert, and E. Waxman, *Astrophys. J.* **654**, 219 (2006), arXiv:astro-ph/0606665 [astro-ph].
- [9] R. Makiya, T. Totani, and M. A. R. Kobayashi, *Astrophys. J.* **728**, 158 (2011), arXiv:1005.1390 [astro-ph.HE].
- [10] Y. Inoue, *Astrophys. J.* **733**, 66 (2011), arXiv:1103.3946 [astro-ph.HE].
- [11] M. Di Mauro, F. Calore, F. Donato, M. Ajello, and L. Latronico, *Astrophys. J.* **780**, 161 (2014), arXiv:1304.0908 [astro-ph.HE].
- [12] M. Ajello *et al.*, *Astrophys. J.* **800**, L27 (2015), arXiv:1501.05301 [astro-ph.HE].
- [13] R. Gould and G. Schröder, *Phys. Rev. Lett.* **16**, 252 (1966).
- [14] S. Camera, M. Fornasa, N. Fornengo, and M. Regis, *Astrophys. J.* **771**, L5 (2013), arXiv:1212.5018 [astro-ph.CO].
- [15] N. Fornengo and M. Regis, *Front. Physics* **2**, 6 (2014), arXiv:1312.4835 [astro-ph.CO].
- [16] V. Allevato, A. Finoguenov, and N. Cappelluti, *Astrophys. J.* **797**, 96 (2014), arXiv:1410.0358 [astro-ph.GA].
- [17] J.-Q. Xia, A. Cuoco, E. Branchini, and M. Viel, *Astrophys. J. Suppl.* **217**, 15 (2015), arXiv:1503.05918 [astro-ph.CO].
- [18] E. Branchini, S. Camera, A. Cuoco, N. Fornengo, M. Regis, M. Viel, and J.-Q. Xia, *Astrophys. J. Suppl.* **228**, 8 (2017), arXiv:1612.05788 [astro-ph.CO].
- [19] M. Bartelmann and P. Schneider, *Phys. Rept.* **340**, 291 (2001), arXiv:astro-ph/9912508 [astro-ph].
- [20] N. Fornengo, L. Perotto, M. Regis, and S. Camera, *Astrophys. J.* **802**, L1 (2015), arXiv:1410.4997 [astro-ph.CO].
- [21] A. Lewis and A. Challinor, *Phys. Rept.* **429**, 1 (2006), arXiv:astro-ph/0601594 [astro-ph].
- [22] M. Shirasaki, S. Horiuchi, and N. Yoshida, *Phys. Rev. D* **90**, 063502 (2014), arXiv:1404.5503 [astro-ph.CO].
- [23] M. Shirasaki, O. Macias, S. Horiuchi, S. Shirai, and N. Yoshida, *Phys. Rev. D* **94**, 063522 (2016), arXiv:1607.02187 [astro-ph.CO].
- [24] T. Troster *et al.*, (2016), 10.1093/mnras/stx365, [Mon. Not. Roy. Astron. Soc. 467, no.3, 2706 (2017)], arXiv:1611.03554 [astro-ph.CO].
- [25] S. Camera, M. Fornasa, N. Fornengo, and M. Regis, *JCAP* **1506**, 029 (2015), arXiv:1411.4651 [astro-ph.CO].
- [26] R. Gilmore, R. Somerville, J. Primack, and A. Dominguez, *Mon. Not. Roy. Astron. Soc.* **422**, 3189 (2012), arXiv:1104.0671 [astro-ph.CO].
- [27] M. Ackermann *et al.* (Fermi-LAT), *Astrophys. J.* **755**, 164 (2012), arXiv:1206.1346 [astro-ph.HE].
- [28] G. Rodighiero *et al.*, *Astron. Astrophys.* **515**, A8 (2010), arXiv:0910.5649 [astro-ph.CO].
- [29] C. J. Willott, S. Rawlings, K. M. Blundell, M. Lacy, and S. A. Eales, *Mon. Not. Roy. Astron. Soc.* **322**, 536 (2001), arXiv:astro-ph/0010419 [astro-ph].
- [30] N. Kaiser and G. Squires, *Astrophys. J.* **404**, 441 (1993).
- [31] G. M. Bernstein and M. Jarvis, *Astron. J.* **123**, 583 (2002), arXiv:astro-ph/0107431 [astro-ph].
- [32] C. Seitz and P. Schneider, *Astron. Astrophys.* **297**, 287 (1995), arXiv:astro-ph/9408050 [astro-ph].
- [33] P. Schneider, *Mon. Not. Roy. Astron. Soc.* **283**, 837 (1996), arXiv:astro-ph/9601039 [astro-ph].
- [34] H. Aihara *et al.* (HSC), *PASJ* **70**, S4 (2018), arXiv:1704.05858 [astro-ph.IM].
- [35] S. Miyazaki *et al.* (HSC), *PASJ* **70**, S1 (2018).
- [36] Y. Komiyama *et al.* (HSC), *PASJ* **70**, S2 (2018).
- [37] H. Furusawa *et al.* (HSC), *PASJ* **70**, S3 (2018).
- [38] R. Mandelbaum *et al.*, (2017), 10.1093/pasj/psx130, arXiv:1705.06745 [astro-ph.CO].

- [39] C. M. Hirata and U. Seljak, *Mon. Not. Roy. Astron. Soc.* **343**, 459 (2003), arXiv:astro-ph/0301054 [astro-ph].
- [40] R. Mandelbaum *et al.*, *Mon. Not. Roy. Astron. Soc.* **450**, 2963 (2015), arXiv:1412.1825 [astro-ph.CO].
- [41] R. Mandelbaum, F. Lanusse, A. Leauthaud, R. Armstrong, M. Simet, H. Miyatake, J. E. Meyers, J. Bosch, S. Miyazaki, and M. Tanaka, (2017), arXiv:1710.00885 [astro-ph.CO].
- [42] M. Tanaka, J. Coupon, B.-C. Hsieh, S. Mineo, A. J. Nishizawa, J. Speagle, H. Furusawa, S. Miyazaki, and H. Murayama, (2017), arXiv:1704.05988 [astro-ph.GA].
- [43] M. Oguri *et al.*, (2017), arXiv:1705.06792 [astro-ph.CO].
- [44] J. Hartlap, P. Simon, and P. Schneider, *Astron. Astrophys.* (2006), 10.1051/0004-6361:20066170, [*Astron. Astrophys.*464,399(2007)], arXiv:astro-ph/0608064 [astro-ph].
- [45] M. Shirasaki and N. Yoshida, *Astrophys.J.* **786**, 43 (2014), arXiv:1312.5032 [astro-ph.CO].
- [46] R. Takahashi, T. Hamana, M. Shirasaki, T. Namikawa, T. Nishimichi, K. Osato, and K. Shiroyama, (2017), arXiv:1706.01472 [astro-ph.CO].
- [47] R. K. Sheth and G. Tormen, *Mon.Not.Roy.Astron.Soc.* **308**, 119 (1999), arXiv:astro-ph/9901122 [astro-ph].
- [48] G. Htsi, M. Gilfanov, and R. Sunyaev, *Astron. Astrophys.* **561**, A58 (2014), arXiv:1304.3717 [astro-ph.CO].
- [49] Y. Inoue and T. Totani, *Astrophys. J.* **702**, 523 (2009), [Erratum: *Astrophys. J.*728,73(2011)], arXiv:0810.3580 [astro-ph].
- [50] K. Bandara, D. Crampton, and L. Simard, *Astrophys. J.* **704**, 1135 (2009), arXiv:0909.0269 [astro-ph.GA].
- [51] S. M. Croom, B. J. Boyle, T. Shanks, R. J. Smith, L. Miller, P. J. Outram, N. S. Loaring, F. Hoyle, and J. da Angela, *Mon. Not. Roy. Astron. Soc.* **356**, 415 (2005), arXiv:astro-ph/0409314 [astro-ph].
- [52] V. Allevato, A. Finoguenov, N. Cappelluti, T. Miyaji, G. Hasinger, M. Salvato, M. Brusa, R. Gilli, G. Zamorani, F. Shankar, J. B. James, H. J. McCracken, A. Bongiorno, A. Merloni, J. A. Peacock, J. Silverman, and A. Comastri, *Astrophys. J.* **736**, 99 (2011), arXiv:1105.0520.
- [53] S. N. Lindsay *et al.*, *Mon. Not. Roy. Astron. Soc.* **440**, 1527 (2014), arXiv:1402.5654 [astro-ph.CO].
- [54] C. M. Urry and P. Padovani, *Publ. Astron. Soc. Pac.* **107**, 803 (1995), arXiv:astro-ph/9506063 [astro-ph].
- [55] F. C. van den Bosch, X. Yang, H. J. Mo, S. M. Weinmann, A. Maccio, S. More, M. Cacciato, R. Skibba, and K. Xi, *Mon. Not. Roy. Astron. Soc.* **376**, 841 (2007), arXiv:astro-ph/0610686 [astro-ph].
- [56] C. Feng, A. Cooray, and B. Keating, *Astrophys. J.* **836**, 127 (2017), arXiv:1608.04351 [astro-ph.CO].
- [57] A. Cuoco, M. Bilicki, J.-Q. Xia, and E. Branchini, (2017), 10.3847/1538-4365/aa8553, [*Astrophys. J. Suppl.*232,10(2017)], arXiv:1709.01940 [astro-ph.HE].
- [58] S. Ando, *JCAP* **1410**, 061 (2014), arXiv:1407.8502 [astro-ph.CO].
- [59] D. Hooper and T. Linden, *Phys.Rev.* **D84**, 123005 (2011), arXiv:1110.0006 [astro-ph.HE].
- [60] M. Ackermann *et al.* (Fermi-LAT), *Phys. Rev.* **D89**, 042001 (2014), arXiv:1310.0828 [astro-ph.HE].
- [61] F. Acero *et al.* (Fermi-LAT), *Astrophys. J. Suppl.* **218**, 23 (2015), arXiv:1501.02003 [astro-ph.HE].
- [62] E. Massaro, P. Giommi, C. Leto, P. Marchegiani, A. Maselli, M. Perri, S. Piranomonte, and S. Scavi, *Astron. Astrophys.* **495**, 691 (2009), arXiv:0810.2206 [astro-ph].
- [63] G. Steigman, B. Dasgupta, and J. F. Beacom, *Phys. Rev. D* **86**, 023506 (2012), arXiv:1204.3622 [hep-ph].
- [64] M. A. Sánchez-Conde and F. Prada, *Mon. Not. Roy. Astron. Soc.* **442**, 2271 (2014), arXiv:1312.1729 [astro-ph.CO].
- [65] M. Shirasaki, S. Horiuchi, and N. Yoshida, *Phys. Rev.* **D92**, 123540 (2015), arXiv:1511.07092 [astro-ph.CO].